Optical and Quantum Communications

Academic and Research Staff
Professor Jeffrey H. Shapiro, Dr. Franco N. C. Wong, Dr. Marco Fiorentino, Dr. Vittorio Giovannetti, Dr. Friedrich König, Dr. Lorenzo Maccone, Dr. Elliott J. Mason, Dr. Gaétan Messin

Graduate Students
Marius A. Albota, Joe Aung, Baris I. Erkmen, Saikat Guha, Shane M. Haas, Francois Impens, Christopher E. Kuklewicz, Mohsen Razavi, Brent J. Yen

Undergraduate Student
Corey Scott

The central theme of our programs has been to advance the understanding of optical and quantum communication, radar, and sensing systems. Broadly speaking, this has entailed: (1) developing system-analytic models for important propagation, detection, and communication scenarios; (2) using these models to derive the fundamental limits on system performance; and (3) identifying, and establishing through experimentation the feasibility of, techniques and devices which can be used to approach these performance limits.

1. Quantum Information and Communication

Sponsors
Air Force Research Laboratory - Cooperative Agreement F30602-01-2-0546
Army Research Office - Grant DAAD-19-00-1-0177
Army Research Office - Grant DAAD-19-01-1-0647
National Reconnaissance Office - Contract NRO-000-00-C-0158
Office of Naval Research - Contract N00014-02-1-0717

Project Staff
Professor Jeffrey H. Shapiro, Dr. Franco N. C. Wong, Dr. Marco Fiorentino, Dr. Vittorio Giovannetti, Dr. Friedrich König, Dr. Lorenzo Maccone, Dr. Elliott J. Mason, Dr. Gaétan Messin, Marius A. Albota, Joe Aung, Saikat Guha, Francois Impens, Christopher E. Kuklewicz, Brent J. Yen

We are embarked on research in the area of quantum information technology whose goal is to enable the quantum-mechanical information transmission, storage, and processing needed for future applications in quantum computing and quantum communication. Our theoretical work in this area has focused on architectural designs for long-distance teleportation and multi-party entanglement transmission, and on novel applications of entanglement. Of particular interest has been the identification of high-performance means for generating the polarization-entangled photons needed for many quantum information applications, including teleportation, entanglement-based quantum positioning and clock synchronization, and quantum secret sharing. Our main experimental work is focused on generation and application of entanglement sources with high brightness and wavelength tunability. In addition, we are interested in novel entanglement sources and their applications in enhanced quantum measurements and quantum teleportation protocols.

Architectural Analysis The preeminent obstacle to the development of quantum information technology is the difficulty of transmitting quantum information over noisy and lossy quantum communication channels, recovering and refreshing the quantum information that is received, and then storing it in a reliable quantum memory. We lead a team of researchers from MIT and Northwestern University that has proposed, analyzed, and is developing the key technological elements of a novel architecture for the singlet-state approach to quantum teleportation [1]. A simple block diagram of this architecture is shown in Fig. 1. It consists of an ultrabright

narrowband source of polarization-entangled photons pairs (*P*), connected to a pair of trapped Rb atom quantum memories (*M*) by transmission through *L*-km-long lengths of standard telecommunication fiber.

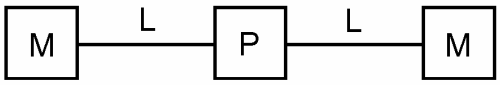

Figure 1. Schematic of long-distance quantum communication system: *P* = ultrabright narrowband source of polarization-entangled photon pairs; *L* = *L* km of standard telecommunication fiber; *M* = trapped atom quantum memory.

Each *M* block in Fig. 1 is a quantum memory in which a single ultracold ^{87}Rb atom is confined by a CO_2-laser trap in an ultra-high vacuum chamber with cryogenic walls within a high-finesse single-ended optical cavity. An abstract representation of the relevant hyperfine levels for such a memory is given in Fig. 2(a). A 795 nm photon in an arbitrary polarization can be absorbed, transferring the qubit from the photon to the degenerate *B* levels of Fig. 2(a), and thence to long-lived storage levels, by coherently driving the *B*-to-*D* transitions. By means of optically-off-resonant (OOR) transitions, the Bell states of two atoms in a single vacuum-chamber trap can be converted into superposition states of one of the atoms. All four Bell measurements needed for the Bennett *et al*. singlet-state teleportation process [2] can then be made, sequentially, by detecting the presence (or absence) of fluorescence as an appropriate sequence of OOR laser pulses is applied to the latter atom. The Bell-measurement results (two bits of classical information) in one memory can be sent to a distant memory, where (at most) two additional OOR pulses are needed to complete the state transformation process. More details on this memory, and its use in teleportation, are given in [3].

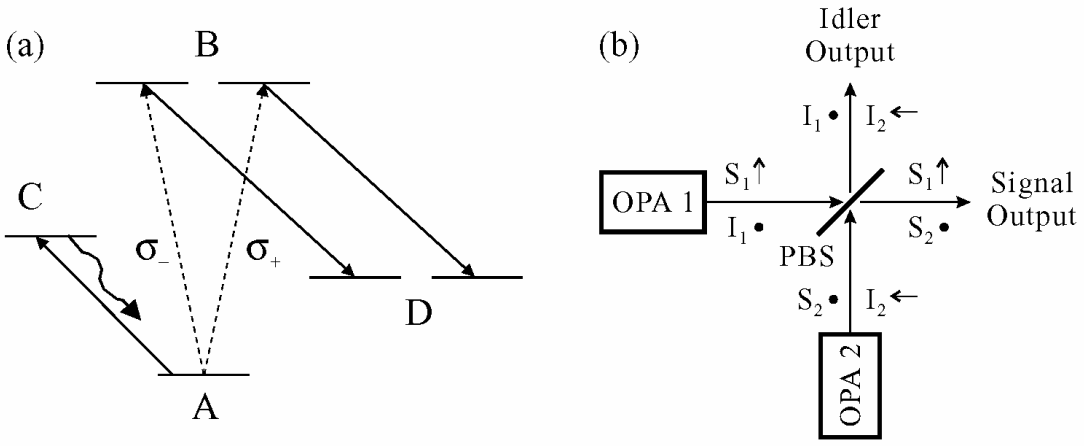

Figure 2. Essential components of singlet-state quantum communication system from Fig. 1. Left (a), simplified atomic-level schematic of the trapped Rb atom quantum memory: *A*-to-*B* transition occurs when one photon from an entangled pair is absorbed; *B*-to-*D* transition is coherently driven to enable storage in the long-lived *D* levels; *A*-to-*C* cycling transition permits nondestructive determination of when a photon has been absorbed. Right (b), ultrabright narrowband source of polarization-entangled photon pairs: each optical parametric amplifier (OPA1 and OPA2) is type-II phase matched; for each optical beam the propagation direction is *z*, and *x* and *y* polarizations are denoted by arrows and bullets, respectively; PBS, polarizing beam splitter.

The *P* block in Fig. 1 is an ultrabright narrowband source of polarization-entangled photon pairs [4], capable of producing ~10^6 pairs/sec in ~30 MHz bandwidth by appropriately combining the signal and idler output beams from two doubly-resonant type-II phase matched optical parametric

amplifiers (OPAs), as sketched in Fig. 2(b). The importance of our resonant approach to entanglement generation is the need to achieve high flux within the narrow linewidth of the Rb atom memory; existing parametric downconverter sources of entanglement are far too broadband to permit useful transmission rates in the Fig. 1 architecture.

During the past year we have augmented and generalized our performance analysis for the preceding teleportation architecture in several ways. First, we have improved our cold-cavity loading analysis of the quantum memories by showing how multi-photon errors can be converted into erasures [5,6], see Fig. 3.

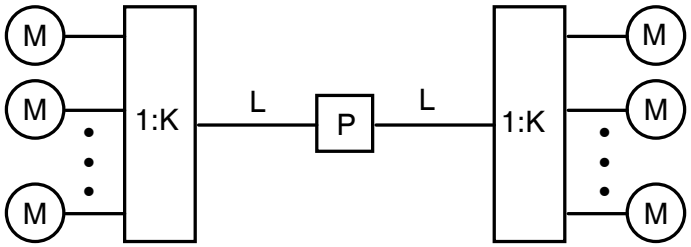

Figure 3. Notional scheme for converting single-photon memory loading errors into erasures. Each single-atom memory block in Fig.1 is replaced with a 1:K fanout and K single-atom memories. A loading event is declared only when exactly one memory at each end of the fiber links has absorbed a photon. All other possibilities are erasures. A single-photon error occurs when a loading event does not store the singlet state that is desired for the teleportation application.

As in our previous work [1], this single-photon error model allows evaluation of the throughput and fidelity achieved in qubit teleportation when the only source of errors is the combined effect of propagation loss and multi-pair emission from the entanglement source. In [5,6] we studied the improvements in fidelity that could be realized with either quantum error-correcting codes (QECCs) or entanglement purification protocols (EPPs). Both of these approaches entail tradeoffs between the fidelity and the teleportation throughput. Examples are shown in Figs. 4 and 5. The five-qubit QECC [7] corrects all single qubit errors and some multi-qubit errors. Figure 4 shows that using this QECC can appreciably improve teleportation fidelity, but this improvement comes at a cost, viz., a factor of five loss in throughput.

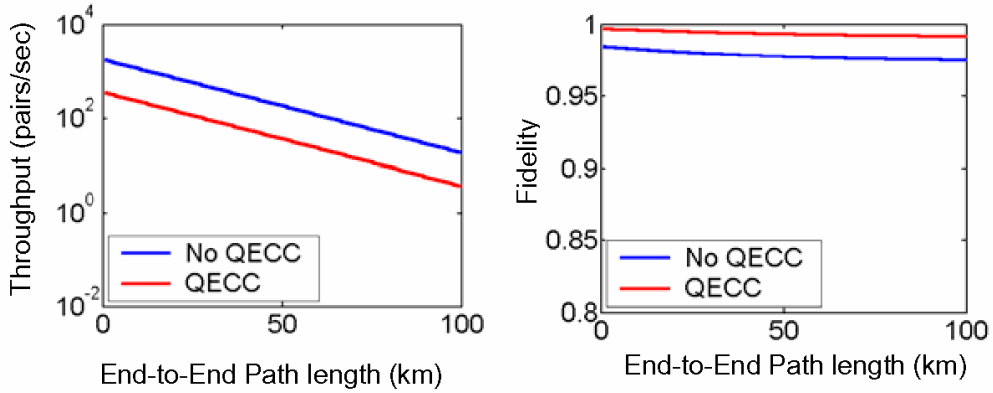

Figure 4. Throughput versus fidelity tradeoff associated with use of the five-qubit QECC. The left panel shows the throughput (in pairs per second) versus end-to-end path length for the Fig. 1 architecture. Here it is assumed that each terminal in Fig. 1 is equipped with an array of Fig. 2(a) memories for sequential loading. The right panel shows the resulting teleportation fidelity versus end-to-end path length. Both panels assume each OPA in Fig. 2(b) is pumped at 1% of its oscillation threshold, 5 dB of fixed loss in each source-to-memory path, and 0.2 dB/km of fiber loss. The upper curve in the left panel and the lower curve in the right panel are for uncoded transmission. The lower curve in the left panel and the upper curve in the right panel assume use of the five-qubit QECC.

Figure 5 shows corresponding results when the one-way hashing EPP is used to improve the teleportation fidelity. An EPP starts from a large number of imperfect entangled pairs, from which a smaller number of more highly-entangled pairs are distilled by means of quantum measurements and classical communication. The one-way hashing EPP [8] has a nonzero asymptotic yield, but a minimum initial fidelity threshold. Because the initial fidelity of the Fig. 1 architecture is quite high, the one-way hashing EPP sacrifices very few pairs to achieve (assuming perfect processing) unity fidelity. However, in order to achieve this outstanding performance, an enormous amount of quantum memory will be needed to reach the asymptotic performance regime.

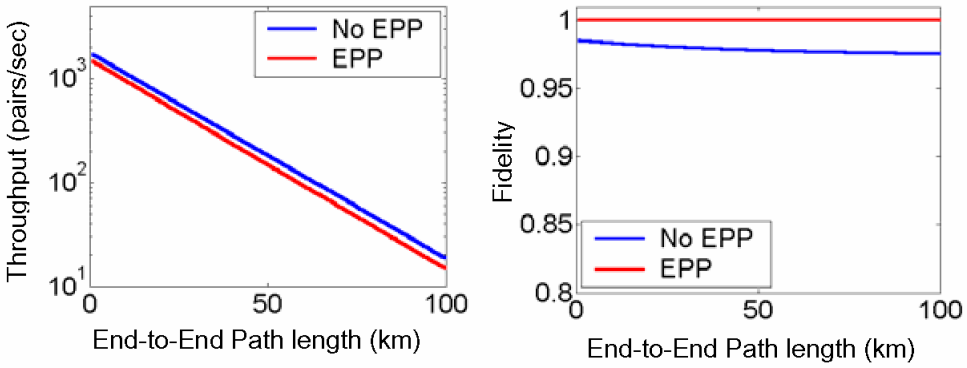

Figure 5. Throughput versus fidelity tradeoff associated with use of the one-way hashing EPP The left panel shows the throughput (in pairs per second) versus end-to-end path length for the Fig. 1 architecture. Here it is assumed that each terminal in Fig. 1 is equipped with an array of Fig. 2(a) memories for sequential loading. The right panel shows the resulting teleportation fidelity versus end-to-end path length. Both panels assume each OPA in Fig. 2(b) is pumped at 1% of its oscillation threshold, 5 dB of fixed loss in each source-to-memory path, and 0.2 dB/km of fiber loss. The upper curve in the left panel and the lower curve in the right panel are for transmission without entanglement purification. The lower curve in the left panel and the upper curve in the right panel assume use of the one-way hashing EPP.

A second architectural area in which we have made significant progress in the past year concerns our extension of the MIT/NU system to permit sharing of multi-party entangled states, specifically the three-party Greenberger-Horne-Zeilinger (GHZ) state, for use in quantum secret sharing. The basic architecture for our GHZ-state communication system, which was first reported in [1], is shown in Figs. 6 and 7.

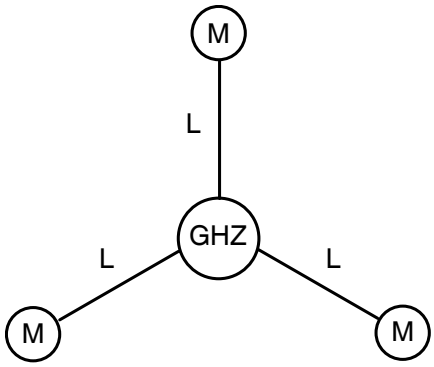

Figure 6. Long-distance communication architecture for GHZ states. GHZ is the source arrangement from either panel of Fig. 7. This source is connected, via *L*-km-long lengths standard telecommunication fiber, to trapped-atom quantum memories. The system uses the memory-loading protocol of the Fig. 1 teleportation architecture.

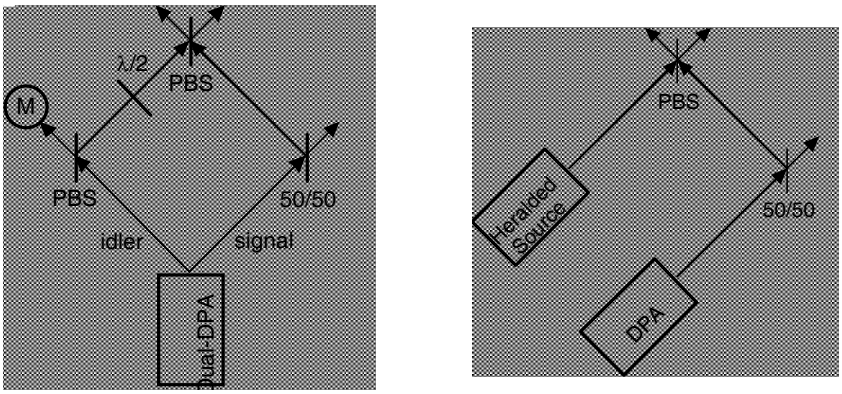

Figure 7. Left panel: degenerate parametric amplifier system for generation of GHZ states. Dual degenerate parametric amplifier (dual-DPA) is a Fig. 2(b) arrangement in which OPAs 1 and 2 operate at frequency degeneracy and are pumped in phase. PBS polarizing beam splitter; *M* trapped-Rb atom quantum memory; λ/2 half-wave plate. Right panel: heralded single-photon source plus degenerate parametric amplifier for GHZ-state generation.

During the past year, we have developed the single-photon error model for the Fig. 6 architecture, and used that model to quantify the performance obtainable in two quantum secret sharing scenarios: one in which classical information is shared, and one in which quantum information is shared. In three-party quantum secret sharing (QSS), Alice, Bob, and Charlie share a collection of GHZ states. By randomly measuring their portions of the shared states, and announcing their measurement bases (but not their results), Alice, Bob, and Charlie can arrive at a shared one-time pad with which Alice can send secret classical messages to Bob and Charlie. This is a secret sharing protocol, because Bob and Charlie must cooperate in order to learn Alice's one-time pad [9]. Figure 8 shows performance results from our analysis [10] of quantum sharing of classical secrets over the Fig. 6 GHZ-state system. As previously seen in [1], for GHZ-state transmission alone, the use of a heralded-plus-DPA source is of great advantage in this classical communication protocol.

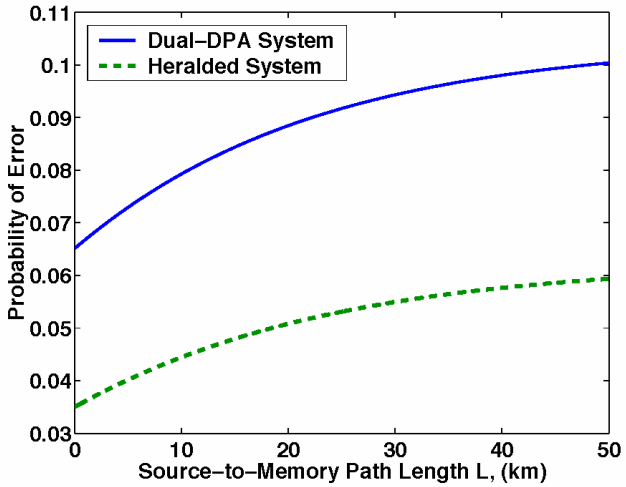

Figure 8. QSS bit error probabilities for the dual-DPA and the heralded-plus-DPA GHZ systems for the QSS protocol. These plots assume each DPA operates at 1% of its oscillation threshold, 5 dB excess loss in each source-to-memory path, and 0.2 dB/km loss in each fiber.

If Alice desires to share a quantum secret, i.e., a qubit, with Bob and Charlie, after they have already shared a GHZ state, she makes Bell state measurements on her secret and her portion of the GHZ state. Labeling the two resulting classical bits as *m* and *n*, she sends *m* to Bob and $m \oplus n$ to Charlie, via secure classical channels. By pooling their quantum and classical information, Bob and Charlie can then arrange for one of them to receive Alice's qubit [9]. Figure 9 shows the resulting fidelity of this QSS protocol when it is realized via the Fig. 6 GHZ-state communication architecture [10]. Again we see the performance advantage of the heralded-plus-DPA source. This figure also shows the fidelity achievable when the five qubit code is employed. Note that the dual-DPA curves for coded and uncoded fidelity cross. This occurs when the prevalence of multiple qubit errors is sufficiently large that use of the five qubit code becomes detrimental to performance. We have also analyzed the use of the multiparty hashing EPP with the quantum secret sharing protocol; see [10] for details.

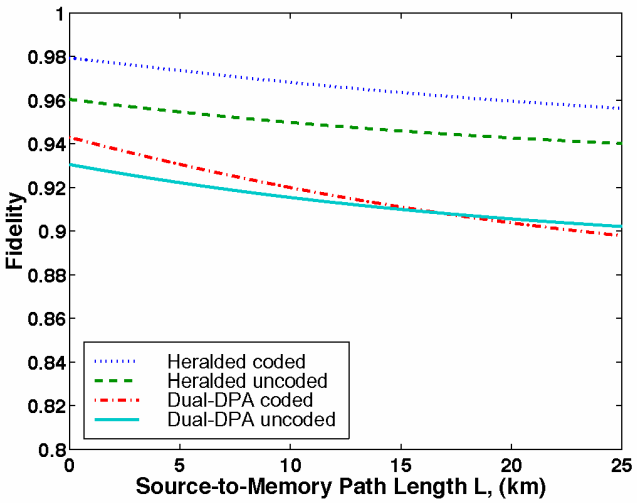

Figure 9. Average fidelity in the QSS protocol. We compare the performance of the dual-DPA and the heralded-plus-DPA GHZ systems with and without use of the five qubit QECC. These plots assume each DPA operates at 1% of its oscillation threshold, 5 dB excess loss in each source-to-memory path, and 0.2 dB/km loss in each fiber.

Single-Beam High-Flux Entanglement Source In recent years most entanglement sources are based on spontaneous parametric downconversion (SPDC) in a noncollinearly propagating, angle phase-matched crystal, such as beta barium borate (BBO) [11]. We have taken a different approach to entanglement generation that is based on periodically-poled potassium titanyl phosphate (PPKTP) with collinear propagation of the pump, signal, and idler fields. Under quasi-phase matching, one can choose to propagate along a principal axis of the PPKTP crystal, thus avoiding undesirable angle walkoff and permitting collinear propagation in long crystals, which can be utilized in cavity configurations for enhancing downconversion efficiency and providing high-brightness narrowband outputs [4]. Furthermore, a single-beam configuration of co-propagating signal and idler photons simplifies the transport of entangled photon pairs. For the current work we have observed quantum interference between the single-beam downconverted photons of a continuous-wave (cw) PPKTP parametric downconverter with a visibility of 99% and a measured coincidence flux of 300/s/mW of pump. We have also measured the Clauser, Horne, Shimony, and Holt (CHSH) form of Bell's inequality violation showing a value of 2.711 ± 0.017.

We have implemented the single-beam downconverter in Fig. 10 using a 10-mm-long hydrothermally-grown PPKTP crystal with a grating period of 9.01 μm that was designed for frequency-degenerate type-II quasi-phase matched operation at a pump wavelength of 397 nm. The output wavelength at 795 nm was chosen to match the transition wavelength of the D_1 line of Rb, which has been proposed for use as a trapped-atom quantum memory for long-distance

teleportation [3]. After passing through a 5-mm-long KTP timing compensator to erase the timing information [12], the output beam was sent through an interference filter centered at 795 nm to restrict the output bandwidth. An adjustable iris was used to control the effective divergence angle of the transmitted beam. A smaller iris increased the depth of field and reduced the spatial resolution of the output photons such that photons generated from any location in the crystal would be spatially indistinguishable.

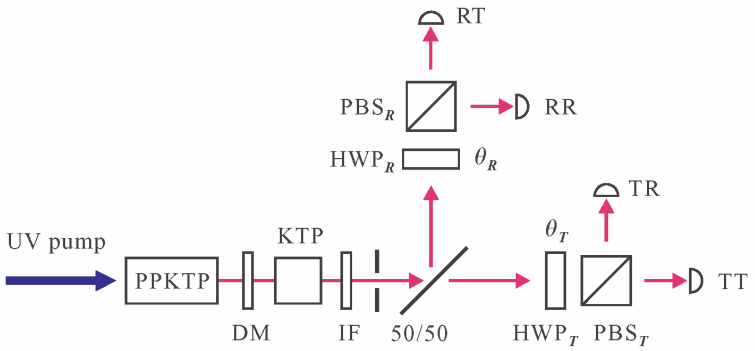

Figure 10. Schematic of experimental setup. The 50/50 beam splitter is removed for quantum interference measurements, which are made with detectors *TT* and *TR*. Detectors *TT* and *RT* are used for Bell's inequality measurements. DM = dichroic mirror; IF = interference filter; HWP = half-wave plate; PBS = polarizing beam splitter.

In the single-beam quantum interference measurements, the 50/50 beam splitter in Fig. 10 was not used. We erased the polarization information of the output photons by rotating the output polarizations by 45° with a half wave plate (HWP$_T$), and the resultant output was the bi-photon state given by

$$|\psi\rangle = \left(|H\rangle_1|H\rangle_2 - |V\rangle_1|V\rangle_2\right)/\sqrt{2},$$

where the photons labeled 1 and 2 were analyzed with a polarization beam splitter (PBS) and detected by single-photon counters labeled *TT* and *TR* in Fig. 10. A null should occur in coincidence measurements, which is equivalent to the coincidence dip in Hong-Ou-Mandel (HOM) interferometry [12,13,14]. The conditional detection efficiency for the hydrothermally-grown PPKTP setup was ~25% for a 3-mm-diameter aperture and a 3-nm interference filter. Figure 11 shows the quantum-interference visibility as a function of the aperture size for four different interference-filter bandwidths. At the aperture size of 1 mm, which is equivalent to a divergence full angle of 5.4 mrad, we observed a visibility of 99 ± 1% for the 1-nm filter. Figure 11 clearly shows that for larger aperture sizes, which correspond to shallower depths of field at the crystal, the visibility is reduced because spatial and spectral indistinguishability was no longer fully maintained. The inset in Fig. 11 shows the detected coincidence rate as a function of the aperture size for the case of the 1-nm filter. At the highest visibility level of 99% obtained with a 1-mm aperture, the measured coincidence rate was ~300/s/mW of pump power, which is one of the highest reported values for an entanglement source at near-unity visibility level [11,15]. Moreover, for an aperture size of 3 mm we measured a flux of over 5000/s/mW of pump while maintaining a visibility of 90%.

We have also obtained polarization entanglement using the setup in Fig. 10 with a flux-grown PPKTP crystal. Each photon of the orthogonally polarized photon pair that is generated from the

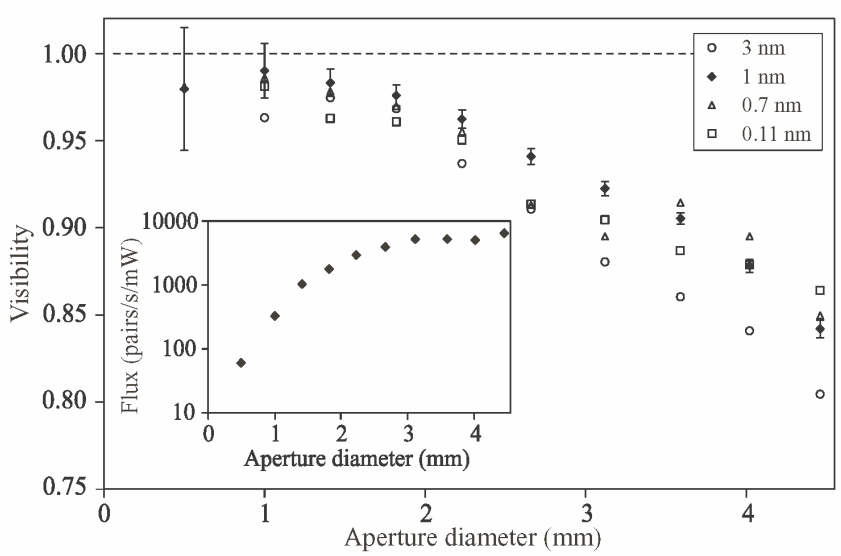

Figure 11. Plot of visibility *V* as a function of aperture diameter for interference filter bandwidths of 3, 1, 0.7, and 0.11 nm. The 0.7-nm filter was composed of two identical 1-nm filters in series. Error bars for the 1-nm data are displayed. Inset plots the detected coincidence flux as a function of the aperture size for the filter bandwidth of 1 nm, showing the trade-off between usable flux and visibility.

PPKTP is equally likely to be transmitted or reflected at the beam splitter. Hence half of the generated pairs yield one photon in the transmitted path and one in the reflected path. If we post-select only these events, the two photons in the two paths are in a polarization-entangled triplet state:

$$|\psi\rangle = \left(|H\rangle_T |V\rangle_R - |V\rangle_T |H\rangle_R\right)/\sqrt{2},$$

where the subscripts *T* and *R* refer to the transmitted and reflected paths of the 50/50 beam splitter, respectively. The quality of the single-beam polarization entanglement can be evaluated by measuring the violation of the CHSH form of Bell's inequality [16]. We have made Bell's inequality measurements using the flux-grown PPKTP downconverter with a 1-nm interference filter and ~10 mW of pump power. Referring to the setup in Fig. 10, the light in the transmitted path and in the reflected path of the 50/50 beam splitter were separately analyzed with a HWP and a PBS. Simultaneous coincidence measurements between different pairs of detectors were taken for two different HWP_T angle settings θ_T of 0 and 22.5° for the transmitted beam. Figure 12 shows the coincidence counts between horizontally polarized photons at the *TT* and *RT* detectors for θ_T = 0 (open circles) and for θ_T = 22.5° (solid circles) and their sinusoidal fits, showing a visibility of 98% and 93%, respectively. From the measurements, we obtain an *S* value of 2.711 ± 0.017, which indicates good polarization entanglement of our PPKTP SPDC source.

High-Flux Source of Nondegenerate Photon Pairs We have also demonstrated an efficient periodically-poled lithium niobate (PPLN) parametric downconverter with collinearly propagating outputs of highly nondegenerate photon pairs [17]. The PPLN downconverter is different from the PPKTP source in several ways. The PPLN downconverter is much more efficient because PPLN has an effective nonlinear coefficient that is nearly 10x larger than that of PPKTP. In our case, using a third-order grating which reduces the effective nonlinearity by a factor of ~3, we have obtained an inferred pair generation of 10^7/s/mW of pump power. The outputs of the PPLN source is highly nondegenerate with outputs at ~800 nm and ~1600 nm. Moreover, the output wavelengths of the PPLN downconverter can be widely tuned over tens of nm by varying the operating temperature of the PPLN crystal at a tuning rate of 1.3 nm/°C. The PPLN source is

particularly useful for implementing the NIT/NU long-distance quantum teleportation protocol [1]. In this protocol, the 795-nm output is for loading a local trapped-Rb quantum memory, and the ~1600-nm output is transmitted through an optical fiber and then frequency translated to 795 nm for loading a remotely located trapped-Rb quantum memory. The wide tunability and high efficiency of this PPLN source make it also useful for many quantum entanglement applications.

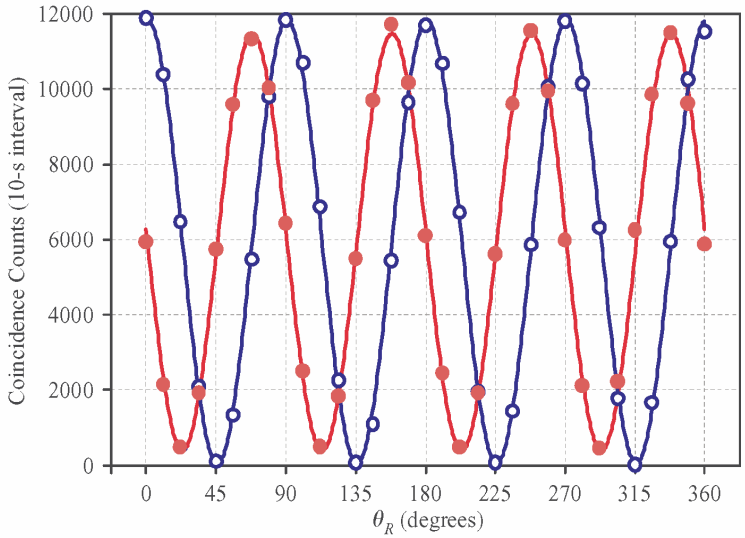

Figure 12. Plot of coincidence counts for θ_T = 0 (open circles) and θ_T = 22.5° (solid circles) in a 10-s counting interval as a function of HWP$_R$ setting θ_R in the reflected path of the 50/50 beam splitter in Fig. 10. Accidental coincidences have been removed in this plot and the sinusoidal fits (solid lines) are used for obtaining visibility and the *S* parameter in the CHSH inequality.

Figure 13 shows a schematic of our PPLN setup for coincidence measurements. The 20-mm-long PPLN crystal with a grating period of 21.6 mm was pumped by a cw frequency-doubled Nd:YVO_4 laser at 532 nm. The crystal was housed in a temperature-stabilized oven at an operating temperature of 140-185°C that allowed wavelength tuning over a large range (idler wavelengths of 1580-1610 nm). The co-polarized, collinearly propagating SPDC outputs were separated by a dispersing prism at Brewster's angle and the signal and idler light were coupled into their respective single mode fibers for spatial filtering and coincidence counting. Detection of an 800-nm signal photon provides a trigger for a gated, thermoelectrically cooled InGaAs avalanche photodiode for single-photon detection of the 1600-nm conjugate idler photon. We achieve a quantum efficiency of ~20% for our InGaAs single photon counters with a dark count probability of ~1.1 x 10^{-3} per 20-ns gate at an operating temperature of -50°C.

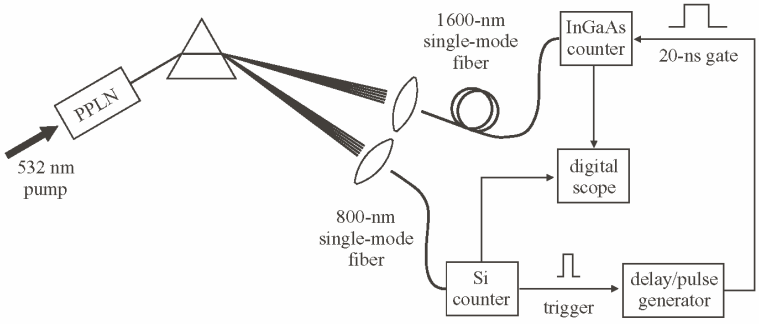

Figure 13. Schematic of experimental setup for coincidence measurements in PPLN downconverter.

Figure 14 shows a histogram of the conditional detection probability η_c of a 1609-nm photon per detected 808-nm photon. It clearly shows that the dark count noise was quite small and the photon pairs were time coincident to within a 4-ns window. The timing accuracy was limited by the 2-ns digitizing time bin and the rise time of the InGaAs detector output pulse (~2 ns). We measured in Fig. 14 η_c of 3.1% within the 4-ns window, limited by the InGaAs detector quantum efficiency of 20%, propagation efficiency of 85%, and the single-mode fiber-coupling and the signal-idler mode-matching efficiency which we infer to be ~18%. More recent improvements in fiber coupling and signal/idler mode matching have boosted η_c to over 5%. This PPLN downconverter system can be extended to include bidirectional pumping and judicious combining of the outputs [4] to efficiently generate nondegenerate polarization-entangled photons.

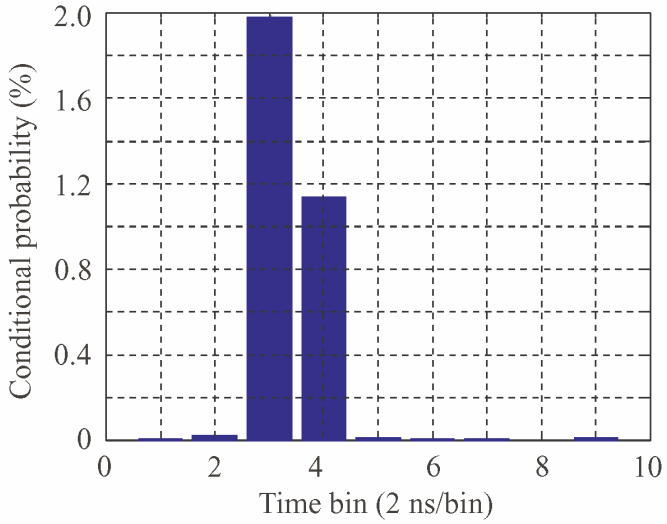

Figure 14. Histogram of idler photon detection probability conditional on signal photon detection in 2-ns time bins over a 20-ns window. Accidental coincidences due to dark counts are barely noticeable outside of the 4-ns coincidence window.

Wideband second harmonic generation under extended phase matching Efficient three-wave mixing with wavelength selectivity is most easily accomplished by use of quasi-phase matching in periodically-poled nonlinear crystals. However, the phase-matching bandwidth is determined only by the dispersion of the nonlinear material, with typical bandwidths of ~1 nm for second harmonic generation (SHG). It is desirable for many applications to have a much wider SHG bandwidth such that angle or temperature tuning is not required for wide tunability. Recently we have proposed the use of an extended phase matching condition for generating coincident-frequency entangled photon pairs in which the signal and idler photons have equal but uncertain frequencies [19]. This condition may be applied to SHG to obtain a phase-matching bandwidth that is larger, by more than an order of magnitude, than the conventional phase-matching result. Applying a Taylor expansion to the usual wave-vector phase matching condition to first order in frequency about the fundamental frequency ω_1 and its SHG frequency $\omega_2 = 2\omega_1$, we obtain the extended phase matching condition [19,20]

$$k_2'(\omega_2) = \frac{k_s'(\omega_1) + k_i'(\omega_1)}{2},$$

where the fundamental wave-vectors k_s and k_i at ω_1 can be the same if they are co-polarized or different if they are orthogonally polarized. The extended phase matching condition is precisely the same as requiring that the group velocity mismatch is zero. The above equation suggests

that for quasi-phase matched interactions, the phase matching bandwidth is set by the second order term in the wave-vector matching. Potentially, this may lead to a substantial increase in the bandwidth.

From Sellmeier equations the extended phase matching condition is found to be satisfied for type-II phase matching in PPKTP at a fundamental wavelength centered at 1580 nm. We have made measurements using a 1-cm-long PPKTP crystal with a 46.1 μm grating and the pump source was a tunable cw laser. For type-II phase matching the input polarization was set at 45° relative to the crystal's *y* and *z* axes. Figure 15 shows the SHG output power as a function of the input wavelength for two orientations of the crystal setting. The narrower phase matching curve corresponds to the exact extended phase matching condition in which the group velocity mismatch is zero, with an observed phase matching bandwidth of ~72 nm. By slightly rotating the PPKTP crystal to induce a small phase mismatch at the center wavelength, the overall bandwidth is increased to ~100 nm. The results show that under the extended phase matching conditions, the phase matching bandwidth is significantly enhanced, which can be particularly useful for wideband nonlinear optics.

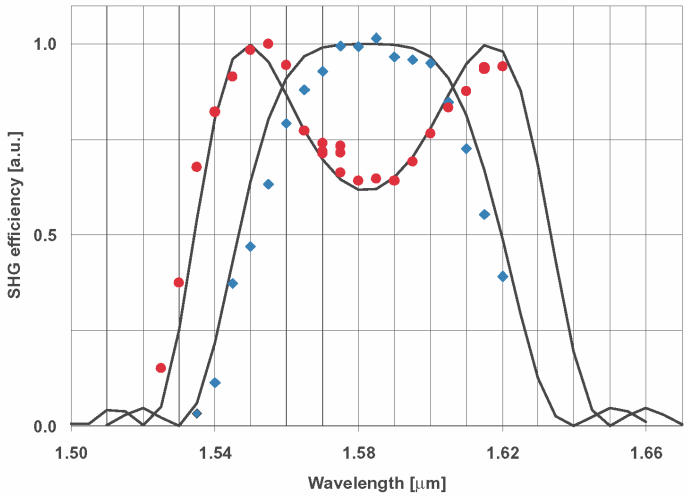

Figure 15. Phase-matching curves of PPKTP under exact extended phase matching condition (blue diamond) and slightly detuned condition (red circle).

2. Atmospheric Optical Communications

Sponsor
Defense Advanced Research Projects Agency - Grant MD1972-00-1-0012

Project Staff
Professor Jeffrey H. Shapiro, Dr. Franco N. C. Wong, Dr. Elliott J. Mason, Baris I. Erkmen, Shane M. Haas, Mohsen Razavi

In future battlefield operations, communications and data networking will play a much more significant role. Properly designed optical communication systems operating over atmospheric paths may be able to provide covert, high burst rate communications with the necessary quick set up and tear down capability. Laser beams propagating through the atmosphere are subject to a wide variety of deleterious effects, including absorption, depolarization, beam spread, angular spread, multipath spread, Doppler spread, and fading. These effects, which represent the combined impact of the atmosphere's molecular constituents, entrained aerosols and hydrometeors, and turbulence-induced refractive index fluctuations, may drastically curtail the

performance of an atmospheric optical link. We are working, in collaboration with Professor Vincent Chan of the Laboratory for Information and Decision Systems, to: provide understanding of battlefield optical communication applications and their implied demands on optical systems; develop architectural constructs that are attainable, but make maximum use of device and subsystem capability to achieve high overall performance; and develop and demonstrate key system concepts in an experimental test bed facility.

The central focus of this program is to address the effects of atmospheric turbulence and how it may be mitigated through the use of diversity techniques in space, time, and frequency. Our work in this regard includes both theoretical and experimental efforts. During the past year, the theory effort has concentrated on three interrelated topics: the error-probability performance of direct-detection diversity receivers using optical preamplification; the capacity of direct detection multiple-input, multiple-output (MIMO) communications; and near-field communication performance. The experimental portion of the program has sought to demonstrate the performance advantage afforded by diversity reception.

Figure 16 shows the structure of three diversity receivers whose performance we have studied [21]. Figure 17 shows some of the results we have obtained. In particular, this figure plots the optical signal-to-noise ratio needed to achieve a 10^{-9} error probability in on-off-keying system versus the turbulence strength, as measured by the logamplitude-fading variance. The left panel applies to the aperture averaging receiver and the right panel to the adaptive optics receiver. In both cases we see that substantial amelioration of the fading results from relatively modest amounts of spatial diversity. We have also shown that very little advantage accrues from using a linear combiner in lieu of the aperture averaging receiver [21].

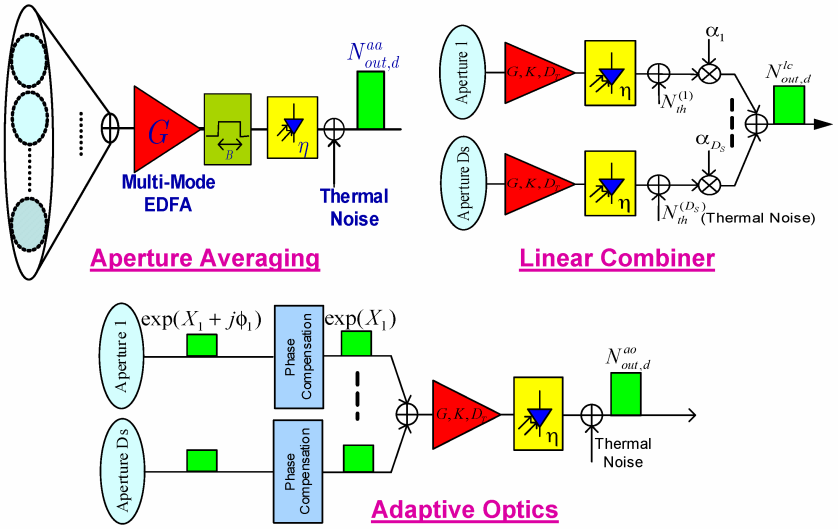

Figure 16. Three classes of direct-detection diversity receivers, all using erbium-doped fiber amplifiers (EDFAs). In each case the receiver aperture consists of multiple atmospheric-turbulence coherence areas. The aperture averaging receiver combines the light from all of these coherence areas on a multi-mode EDFA prior to direct detection. The linear combiner uses a single-mode EDFA (gain G, noise factor K, and D_T temporal modes) for each coherence area followed by direct detection, and weighted linear combining. The adaptive optics receiver first compensates for the turbulence-induced phase differences between the coherence areas, permitting the use of a single-mode EDFA prior to direct detection. All three receivers are subject to post-detection additive thermal noise.

Our derivation of MIMO single-user communication capacity for the turbulent atmosphere assumes the communication configuration shown in Fig. 18. In previous work [22] we developed tight bounds on the MIMO capacity under peak and average power constraints when the path

gains were known and nonrandom. We have since extended that analysis to obtain both the ergodic and outage capacities when the path gains are the independent, identically distributed, lognormal fades associated with atmospheric turbulence. Figure 19 shows our results for the ergodic capacity [23]. Although we could not obtain exact results, the bounds we have found are quite tight.

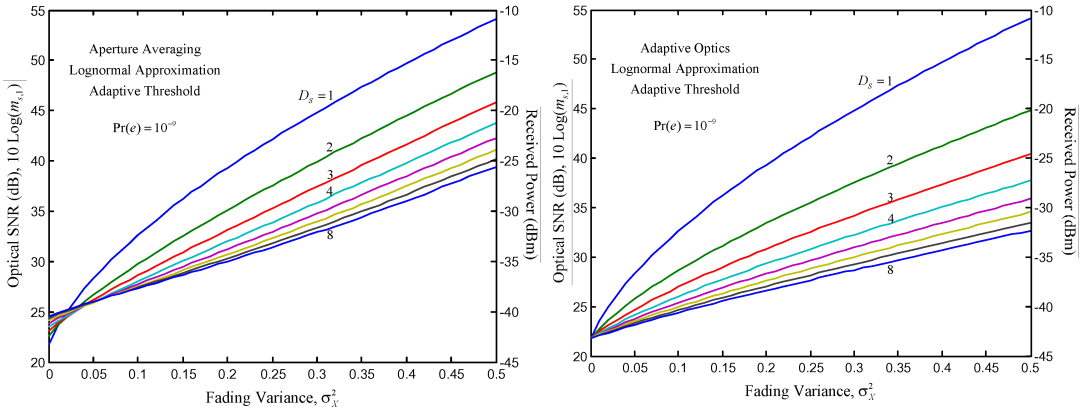

Figure 17. Optical signal-to-noise ratios needed to obtain 10^{-9} bit error probability in on-off-keyed optical communication through atmospheric turbulence plotted versus logamplitude variance. Left panel: aperture averaging receiver. Right panel: adaptive optics receiver.

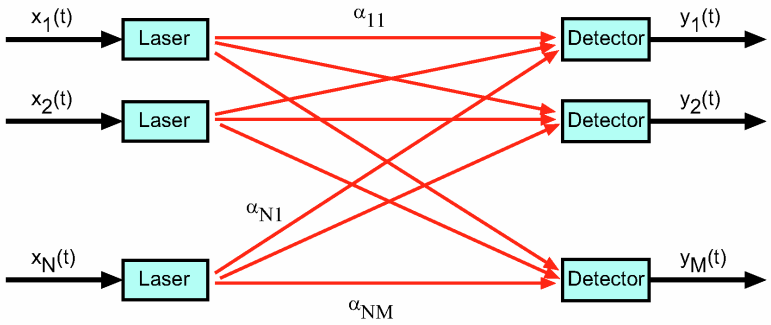

Figure 18. Block diagram of the multiple-input, multiple-output, single-user Poisson channel with turbulence-induced fading. A single-user information source modulates the power from *N* laser sources using waveforms $\{x_n(t)\}$. These lasers couple power to *M* shot-noise limited (Poisson statistics) photodetectors via the independent, identically distributed, lognormal path gains $\{\alpha_{nm}\}$. The single-user receiver decodes the transmitted information from observations of the conditional Poisson processes $\{y_m(t)\}$.

Almost all work on optical communication through atmospheric turbulence assumes operation in the far-field power transfer regime, wherein only a small fraction of the transmitted power is intercepted by the receiver aperture. For line-of-sight terrestrial paths, however, it is easily possible to operate in the near-field power transfer regime, in which almost all of the transmitted power couples to the receiver aperture when there is no turbulence. Previously [24], we have shown that similar far-field and near-field power transfer regimes exist for the turbulent atmosphere. In the near field, there are multiple spatial modes at the transmitter that couple tightly to the receiver. Ordinarily, near-field operation is considered only for imaging scenarios, because within the near field there are multiple spatial modes that efficiently couple power from the transmitter to the receiver. The number of such modes is then the number of pixels resolved by the imaging system. Our interest in near-field communication through atmospheric turbulence derives from the possibility it affords for minimizing transmitter power, hence extending the

lifetime of battery-operated field equipment and minimizing the likelihood of eavesdropping on the communication link by unauthorized personnel. Thus far we have derived loose bounds on the binary error probability of direct detection and coherent detection near-field communications. We are working to tighten these results.

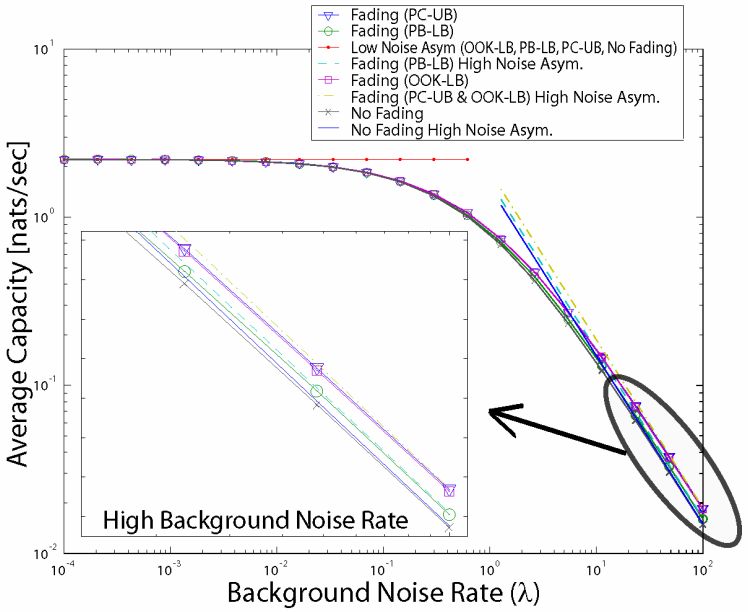

Figure 19. The average capacity without average power constraint for two identical transmitters and three receivers as a function of background noise power. The parallel-channel upper bound (PC-UB) and OOK lower bound (OOK-LB) are shown along with the photon-bucket lower bound (PB-LB). All of these bounds have been averaged over 20,000 channel realizations of moderate fading intensity. The average capacity results for the high and low noise regimes are shown as lines, along with the capacity of a unit path gain channel and its high noise asymptote.

In addition to the theoretical treatment of atmospheric optical communication, we are developing an experimental test bed to supplement and support the analytical work. We have completed the setup of an OC-24 (1.2-Gb/s) open-air link between a laboratory on the 4th floor of Building 35 and the roof of Building N10, spanning an effective path length of ~250 m, as shown schematically in Fig. 20. A cw laser at one of the ITU grid wavelengths (~1559 nm) is externally modulated with a bias-free modulator before being launched into free space with a 10x telescope. The output power is adjustable with the use of a variable fiber-optic attenuator located after the modulator. A high-quality 20-cm-diameter flat high reflector is mounted on a mirror mount inside a wooden box that is securely situated on the roof of Building N10. The transmitted light is reflected at the rooftop mirror back to the laboratory for detection. We estimate that the return beam has a beam diameter of ~25 cm. Portions of the returned light are collected by two optical diversity receivers that are spatially separated by 18 cm to ensure low correlations in turbulence-induced fading.

Figure 20 shows the components of one of the two optical receivers. A 2.5-cm-diameter lens with a focal length of 10 cm is used to focus the incoming light, which is approximately flat top within the lens aperture, into a single-mode optical fiber. For output power of 2 dBm, we typically capture about -37 dBm per receiver. The receiver signal is then optical amplified with an erbium doped fiber amplifier (EDFA) to boost its signal strength, narrowband filtered to reduce the amplified spontaneous emission noise from the EDFA, and detected using a pin photodiode. The two resultant electrical signals from the diversity receivers are amplified, low-pass filtered, and combined wth equal weight for bit-error rate analysis. We also monitored the detected power levels at the p-i-n diode detectors to record the fluctuations at the input aperture of the two optical receivers. We have observed that the fading statistics are largely uncorrelated. We have evaluated the performance of the two-receiver diversity reception system and significant

improvement has been observed with the system compared with a single receiver. The improvement in bit-error rates is due partly to the collection of twice the optical power of a single receiver. It is also partly a result of the compensating capability of diversity reception systems, in which uncorrelated mild fading at the two receiver apertures has a low probability of simultaneous loss of signal in both channels. Figure 21 shows plots of the measured bit-error rates as a function of the single-receiver power and the theoretical curves corresponding to the measured fading statistics. The plots clearly show the advantages of the 2-receiver diversity scheme and the relatively close fit between experiment and theory. We will soon evaluate other diversity schemes such as transmitter diversity.

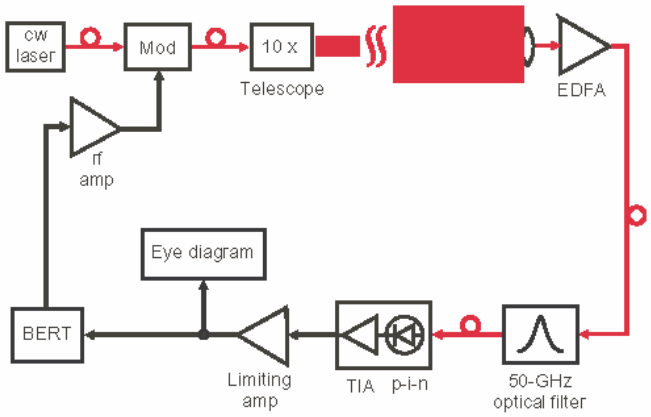

Figure 20. Schematic of 1.2-Gb/s free-space link. Mod: OOK modulator; EDFA: erbium-doped fiber amplifier; TIA: transimpedance amplifier; BERT: bit error rate tester.

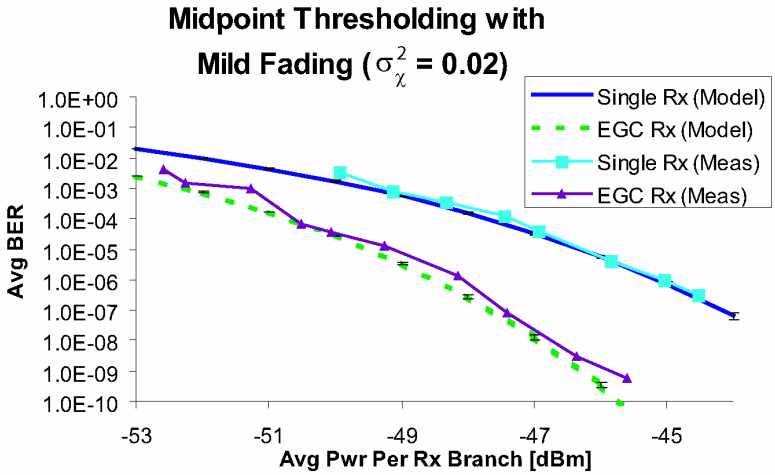

Figure 21. Bit error rate (BER) measurements versus received optical power at the input of EDFA for single receiver and equal-gain-combining (EGC) two-receiver diversity reception. Also shown are theoretical error probability results, based on our system calibration and the measured logamplitude variance.

References

1. J. H. Shapiro, “Architectures for Long-Distance Quantum Communication,” *New J. Phys*. 4, 47.1-47.18 (2002).

2. C. H. Bennett, G. Brassard, C. Crépeau, R. Jozsa, A. Peres, and W. K. Wootters, “Teleporting and Unknown Quantum State via Dual Classical and Einstein-Podolsky-Rosen Channels,” *Phys. Rev. Lett*. 70, 1895-1899 (1993).

3. S. Lloyd, M. S. Shahriar, J. H. Shapiro, and P. R. Hemmer, “Long-Distance Unconditional Teleportation of Atomic States via Complete Bell State Measurements,” *Phys. Rev. Lett*. 87, 167903 (2001).

4. J. H. Shapiro and N. C. Wong, “An Ultrabright Narrowband Source of Polarization-Entangled Photon Pairs,” *J. Opt. B: Quantum Semiclass*. Opt. 2, L1-L4 (2000).

5. J. Aung, *Quantum Error Modeling and Correction in Long Distance Teleportation using Singlet States*, S.M. thesis, Department of Electrical Engineering and Computer Science, MIT, 2002.

6. J. H. Shapiro, J. Aung, and B. J. Yen, “Quantum Error Models and Error Mitigation for Long-Distance Teleportation Architectures,” *Proceedings of the Feynman Festival*, College Park, MD, August 2002, quant-ph/0211086.

7. R. Laflamme, C. Miquel, J. P. Paz, and W. H. Zurek, “Perfect Quantum Error Correcting Code,” *Phys. Rev. Lett*. 77, 198-201 (1996).

8. C. H. Bennett, D. P. DiVincenzo, J. Smolin, and W. K. Wootters, “Mixed State Entanglement and Quantum Error Correction,” Phys. Rev. A 54, 3824-3851 (1996).

9. M. Hillery, V. Buzek, and A. Berthiaume, “Quantum Secret Sharing,” *Phys. Rev. A* 59, 1829-1834 (1999).

10. B. J. Yen and J. H. Shapiro, “Error Models and Error Mitigation for Long-Distance, High-Fidelity Quantum Secret Sharing,” *Proc. SPIE* 5111, 104-117 (2003).

11. P. G. Kwiat, E. Waks, A. G. White, I. Appelbaum, and P. H. Eberhard, “Ultrabright Source of Polarization-Entangled Photons,” *Phys. Rev. A* 60, R773-R776 (1999).

12. M. H. Rubin, D. N. Klyshko, Y. H. Shih, and A. V. Sergienko, "Theory of Two-Photon Entanglement in Type-II Optical Parametric Down-Conversion," *Phys. Rev. A* 50, 5122-5133 (1994).

13. C. K. Hong, Z. Y. Ou, and L. Mandel, "Measurement of Subpicosecond Time Intervals between 2 Photons by Interference," *Phys. Rev. Lett.* 59, 2044-2047 (1987).

14. C. E. Kuklewicz, E. Keskiner, F. N. C. Wong, and J. H. Shapiro, “A High-Flux Entanglement Source Based on a Doubly-Resonant Optical Parametric Amplifier,” *J. Opt. B: Quantum Semiclass. Opt.* 4, S162-S168 (2002).

15. C. Kurtsiefer, M. Oberparleiter, and H. Weinfurter, "High-Efficiency Entangled Photon Pair Collection in Type-II Parametric Fluorescence," *Phys. Rev. A* 64, 023802 (2001).

16. J. F. Clauser, M. A. Horne, A. Shimony, and R. A. Holt, "Proposed Experiment to Test Local Hidden-Variable Theories," *Phys. Rev. Lett.* 23, 880-884 (1969).

17. E. J. Mason, M. A. Albota, F. König, and F. N. C. Wong, "Efficient Generation of Tunable Photon Pairs at 0.8 and 1.6 □m," *Opt. Lett*. 27, 2115-2117 (2002).

18. V. Giovannetti, L. Maccone, J. H. Shapiro, and F. N. C. Wong, "Generating Entangled Two-Photon States with Coincident Frequencies," *Phys. Rev. Lett*. 88, 183602 (2002).

19. V. Giovannetti, L. Maccone, J.H. Shapiro, and F.N.C. Wong, "Extended Phase-Matching Conditions for Improved Entanglement Generation," *Phys. Rev. A* 66, 043813 (2002).

20. J. H. Shapiro, "Imaging and Optical Communication through Atmospheric Turbulence," in *Laser Beam Propagation in the Atmosphere*, ed. J. W. Strohbehn (Springer, Berlin, 1978).

21. M. Razavi and J. H. Shapiro, "Wireless Optical Communication via Diversity Reception and Optical Preamplification," *Digest of 2003 IEEE International Conference on Communications*, Anchorage, AK, 2003.

22. S. M. Haas and J. H. Shapiro, "Capacity of the Multiple-Input, Multiple-Output Poisson Channel," in B. Pasik-Duncan, ed.*, Stochastic Theory and Control, Proceedings of a Workshop held in Lawrence, Kansas, October 18-20, 2001* (Springer-Verlag, Berlin,2002).

23. S. M. Haas and J. H. Shapiro, "Capacity of Wireless Optical Communications*," IEEE J. Sel. Areas in Commun*., forthcoming.

24. J. H. Shapiro, "Normal-Mode Approach to Wave Propagation in the Turbulent Atmosphere," *Appl. Opt*. 13, 2614-2619 (1974).

Publications

Journal Articles, Published

S. Lloyd, J. H. Shapiro, and F. N. C. Wong, "Quantum Magic Bullets by Means of Entanglement," *J. Opt. Soc. Am. B* 19, 312-318 (2002).

C. E. Kuklewicz, E. Keskiner, F. N. C. Wong, and J. H. Shapiro, "A High-Flux Entanglement Source Based on a Doubly-Resonant Optical Parametric Amplifier," *J. Opt. B: Quantum Semiclass. Opt.* 4, S162-S168 (2002).

V. Giovannetti, S. Lloyd, L. Maccone, and F .N. C. Wong, "Clock Synchronization and Dispersion," *J. Opt. B: Quantum and Semiclassical Opt*. 4, S415-S417 (2002).

V. Giovannetti, L. Maccone, J. H. Shapiro, and F. N. C. Wong, "Generating Entangled Two-Photon States with Coincident Frequencies," *Phys. Rev. Lett*. 88, 183602 (2002).

J. H. Shapiro, "Architectures for Long-Distance Quantum Teleportation," *New J. Phys*. 4, 47.1-47.18 (2002).

E. J. Mason, M. A. Albota, F. König, and F. N. C. Wong, "Efficient Generation of Tunable Photon Pairs at 0.8 and 1.6 □m," *Opt. Lett*. 27, 2115-2117 (2002).

V. Giovannetti, L. Maccone, J. H. Shapiro, and F. N. C. Wong, "Extended Phase-Matching Conditions for Improved Entanglement Generation," *Phys. Rev. A* 66, 043813 (2002).

A. Lvovsky and J. H. Shapiro, "Nonclassical Character of Statistical Mixtures of the Single-Photon and Vacuum Optical States," *Phys. Rev. A* 65, 033830 (2002).

S. M. Haas, J. H. Shapiro, and V. Tarokh, "Space-Time Codes for Wireless Optical Communications," *EURASIP J. on Appl. Signal Proc*. 3, 211-220 (2002).

Journal Articles, Accepted for Publication

C.-P. Yeang, C. Cho, and J. H. Shapiro, "A Target-Recognition Theory of SAR Imagery using Electromagnetics-Based Signatures," *Opt. Engr*., forthcoming.

S. M. Haas and J. H. Shapiro, "Capacity of Wireless Optical Communications*," IEEE J. Sel. Areas in Commun*., forthcoming.

Journal Articles, Submitted for Publication

M. Razavi and J. H. Shapiro, "Wireless Optical Communications via Diversity Reception and Optical Preamplification," submitted to *IEEE Trans. on Wireless Commun*.

Book/Chapters in Books

J. H. Shapiro and O. Hirota, eds., *Proceedings of the Sixth International Conference on Quantum Communication, Measurement and Computing* (Rinton Press, Princeton, 2003).

Meeting Papers, Presented

J. Aung and J. H. Shapiro, "Quantum Error Modeling and Correction in Long Distance Teleportation using Singlet States," paper presented at *the 2002 Progress in Electromagnetic theory Research Symposium*, Cambridge, MA, July 2002.

F. König, E. J. Mason, M. A. Albota, and F. N. C. Wong, "Efficient Source of Tunable Nondegenerate Photon Pairs at 800 nm and 1600 nm using Periodically-Poled Lithium Niobate," paper presented at the *3rd European Quantum Information Processing and Communication Workshop*, Dublin, Ireland, September 2002.

J. H. Shapiro, "Architectures for Long-Distance Quantum Teleportation," paper presented at the *2002 Annual Meeting of the Optical Society of America*, Orlando, FL, October 2002.

Meeting Papers, Published

C. E. Kuklewicz, G. Messin, F. N. C. Wong, and J. H. Shapiro, "Quantum Interference from a High-Flux Collinear PPKTP Parametric Downconverter," *Digest of Quantum Electronics and Laser Science Conference*, Long Beach, CA, May 2002, p. 28.

S. M. Haas and J. H. Shapiro, "Capacity of the Multiiple-Input, Multiple-Output Channel," Digest of the 2002 IEEE International Symposium on Information Theory, Lausanne Switzerland, July 2002.

E. J. Mason, M. A. Albota, F. König, and F. N. C. Wong, " A Frequency-Nondegenerate Entanglement Source using Periodically Poled Lithium Niobate," in J. H. Shapiro and O. Hirota, eds., *Proceedings of the Sixth International Conference on Quantum Communication, Measurement and Computing* (Rinton Press, Princeton, 2003), p. 107-110.

J. H. Shapiro, "Generating Quantum Interference and Polarization Entanglement wit Optical Parametric Amplifiers," in J. H. Shapiro and O. Hirota, eds., *Proceedings of the Sixth International Conference on Quantum Communication, Measurement and Computing* (Rinton Press, Princeton, 2003), p 153-158.

V. Giovannetti, L. Maccone, J. H. Shapiro, and F. N. C. Wong, "Maximal Entanglement Generation via Pulsed Parametric Downconversion," in J. H. Shapiro and O. Hirota, eds., *Proceedings of the Sixth International Conference on Quantum Communication, Measurement and Computing* (Rinton Press, Princeton, 2003), p 163-166.

J. H. Shapiro, "Coincidence Dips and Revivals from a Type-II Optical Parametric Amplifier," *Digest of Nonlinear Optics*, Maui, HI, July 2002, pp. 440-442.

M. A. Albota, F. König, C. E. Kuklewicz, E. J. Mason, G. Messin, J. H. Shapiro, and F. N. C. Wong, "High-Flux Entanglement Sources using Periodically-Poled Nonlinear Crystals," *Digest of Nonlinear Optics*, Maui, HI, July 2002, pp. 443-445.

J. H. Shapiro, J. Aung, and B. J. Yen, "Quantum Error Models and Error Mitigation for Long-Distance Teleportation Architectures," *Proceedings of the Feynman Festival*, College Park, MD, August 2002, quant-ph/0211086.

Theses

E. J. Mason, *Applications of Optical Parametric Downconversion: I. Self-Phase Locking; II. Generation of Entangled Photon Pairs in Periodically-Poled Lithium Niobate*, Ph.D. thesis, Department of Electrical Engineering and Computer Science MIT, 2002.

M. A. Albota, *Single-Photon Detection of 1.55 μm Entangled Light and Frequency Upconversion in Periodically-Poled Lithium Niobate for Quantum Communication*, S.M. thesis, Department of Electrical Engineering and Computer Science, MIT, 2002

J. Aung, *Quantum Error Modeling and Correction in Long Distance Teleportation using Singlet States*, M.S. thesis, Department of Electrical Engineering and Computer Science, MIT, 2002.